Resource

Cell Metabolism

Exploring Metabolic Configurations of Single Cells within Complex Tissue Microenvironments

Graphical Abstract

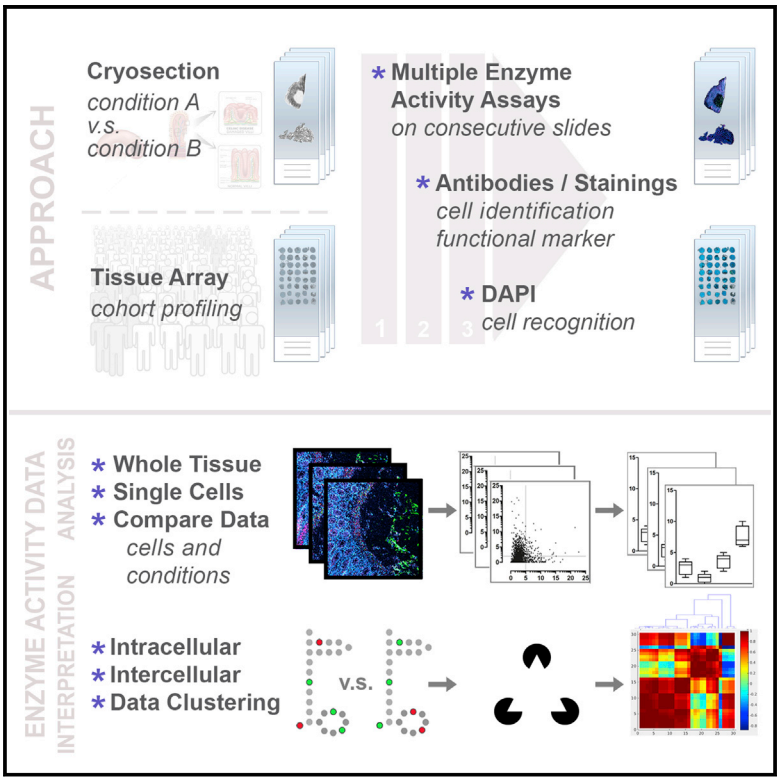

Highlights

- A method to assess intra- and intercellular metabolic configurations *in situ*
- Monitoring metabolic steady states and dynamic responses to physiological stimuli
- Assessing metabolic reconfigurations of immune cell populations in human colon cancer
- Identification of metabolically defined ductal carcinoma patient subgroups

Authors

Anne Miller, Csörsz Nagy, Bernhard Knapp, ..., Michael Bergmann, Oswald Wagner, Arvand Haschemi

Correspondence

arvand.haschemi@meduniwien.ac.at

In Brief

Miller et al. developed a method to assess the metabolic configuration of single cells in intact tissue microenvironments. They quantify multiple enzymatic activities combined with subsequent cell type identification to reveal intra- and intercellular metabolic configurations in cancer patients.

Miller et al., 2017, Cell Metabolism *26*, 788–800
November 7, 2017
http://dx.doi.org/10.1016/j.cmet.2017.08.014

CellPress

Cell Metabolism
Resource

Exploring Metabolic Configurations of Single Cells within Complex Tissue Microenvironments

Anne Miller,[1] Csörsz Nagy,[1] Bernhard Knapp,[2,7] Johannes Laengle,[3] Elisabeth Ponweiser,[1] Marion Groeger,[4] Philipp Starkl,[5,6] Michael Bergmann,[3] Oswald Wagner,[1] and Arvand Haschemi[1,8,*]

[1]Department of Laboratory Medicine, Medical University of Vienna, 1090 Vienna, Austria
[2]Department of Statistics, Protein Informatics Group, University of Oxford, OX13SY Oxford, UK
[3]Division of General Surgery, Department of Surgery, Comprehensive Cancer Center Vienna, Medical University of Vienna, 1090 Vienna, Austria
[4]Core Facility Imaging, Skin and Endothelium Research Division, Medical University of Vienna, 1090 Vienna, Austria
[5]CeMM—Research Center for Molecular Medicine of the Austrian Academy of Sciences, 1090 Vienna, Austria
[6]Department of Medicine I, Laboratory of Infection Biology, Medical University of Vienna, 1090 Vienna, Austria
[7]Present address: Faculty of Medicine and Health Sciences, International University of Catalonia, 08017 Barcelona, Spain
[8]Lead Contact
*Correspondence: arvand.haschemi@meduniwien.ac.at
http://dx.doi.org/10.1016/j.cmet.2017.08.014

SUMMARY

Over the past years, plenty of evidence has emerged illustrating how metabolism supports many aspects of cellular function and how metabolic reprogramming can drive cell differentiation and fate. Here, we present a method to assess the metabolic configuration of single cells within their native tissue microenvironment via the visualization and quantification of multiple enzymatic activities measured at saturating substrate conditions combined with subsequent cell type identification. After careful validation of the approach and to demonstrate its potential, we assessed the intracellular metabolic configuration of different human immune cell populations in healthy and tumor colon tissue. Additionally, we analyzed the intercellular metabolic relationship between cancer cells and cancer-associated fibroblasts in a breast cancer tissue array. This study demonstrates that the determination of metabolic configurations in single cells could be a powerful complementary tool for every researcher interested to study metabolic networks *in situ*.

INTRODUCTION

The adaptive cellular heterogeneity of tissue, along with the plasticity of individual cells, defines the specialized architecture of a tissue microenvironment. The metabolic processes within such biological systems appear to be very complex and difficult to understand as such processes do not only sustain cell-type-specific energy demands, but may also be directly involved in cell signaling and in shaping the dynamic tissue architectures (Cairns et al., 2011; Ghesquière et al., 2014; Hanahan and Weinberg, 2011; Kamphorst and Gottlieb, 2016; Nakazawa et al., 2016). Cancer biology is a prime example that demonstrates the importance of spatially resolved information on cellular metabolism. Particularly, the interaction of cancer cells with stromal and infiltrating immune cells appears to have a tremendous impact on disease progression and patient survival (Fridman et al., 2012; Gajewski et al., 2013; Gascard and Tlsty, 2016; Kalluri, 2016; Motz and Coukos, 2013; Turley et al., 2015). Furthermore, recent insights from immunometabolism research indicate that most immune cells employ specific and intrinsic metabolic reprogramming mechanisms to bioenergetically adapt while polarizing into various activation or effector states (Loftus and Finlay, 2016; O'Neill et al., 2016; O'Neill and Pearce, 2016; Van den Bossche et al., 2017).

The broad repertoire of available methods to investigate cellular metabolism can be grouped into (1) tools to monitor the general parameters or endpoints of metabolism (i.e., oxygen consumption and extracellular acidification rates), (2) quantification of extra- and intracellular metabolites by mass spectrometry (i.e., steady-state metabolomics), and (3) biochemical characterization of metabolic enzymes, which form the scaffold of metabolic pathways (i.e., enzyme activity assays). In a cellular context, both metabolite bioavailability and enzyme activities co-define metabolic activity. This metabolic activity, also known as metabolic flux, can therefore be seen as the consequence of (2) and (3) and as an explanation for effects observed by (1). The dynamics of metabolic flux within cellular entities can be assessed by stationary and non-stationary metabolic flux analyses that involve, e.g., ^{13}C-labled carbon substrates (TeSlaa and Teitell, 2014). The above-mentioned tools are widely applied by researchers and clinicians to determine metabolic properties of cultured and isolated cells, crude tissue homogenates, or biofluids. Indirect calorimetry and tools from nuclear medicine, including functional imaging techniques such as positron emission tomography or magnetic resonance imaging, complement the methodological toolbox for the investigation of metabolic processes also *in vivo*. However, to our knowledge, none of the above-mentioned techniques are currently used in single-cell approaches to characterize the metabolic signatures of cells within their native microenvironment. In fact, all of these tools currently lack the spatial resolution, which is a prerequisite to decipher the metabolic signature of complex, heterogeneous tissues.

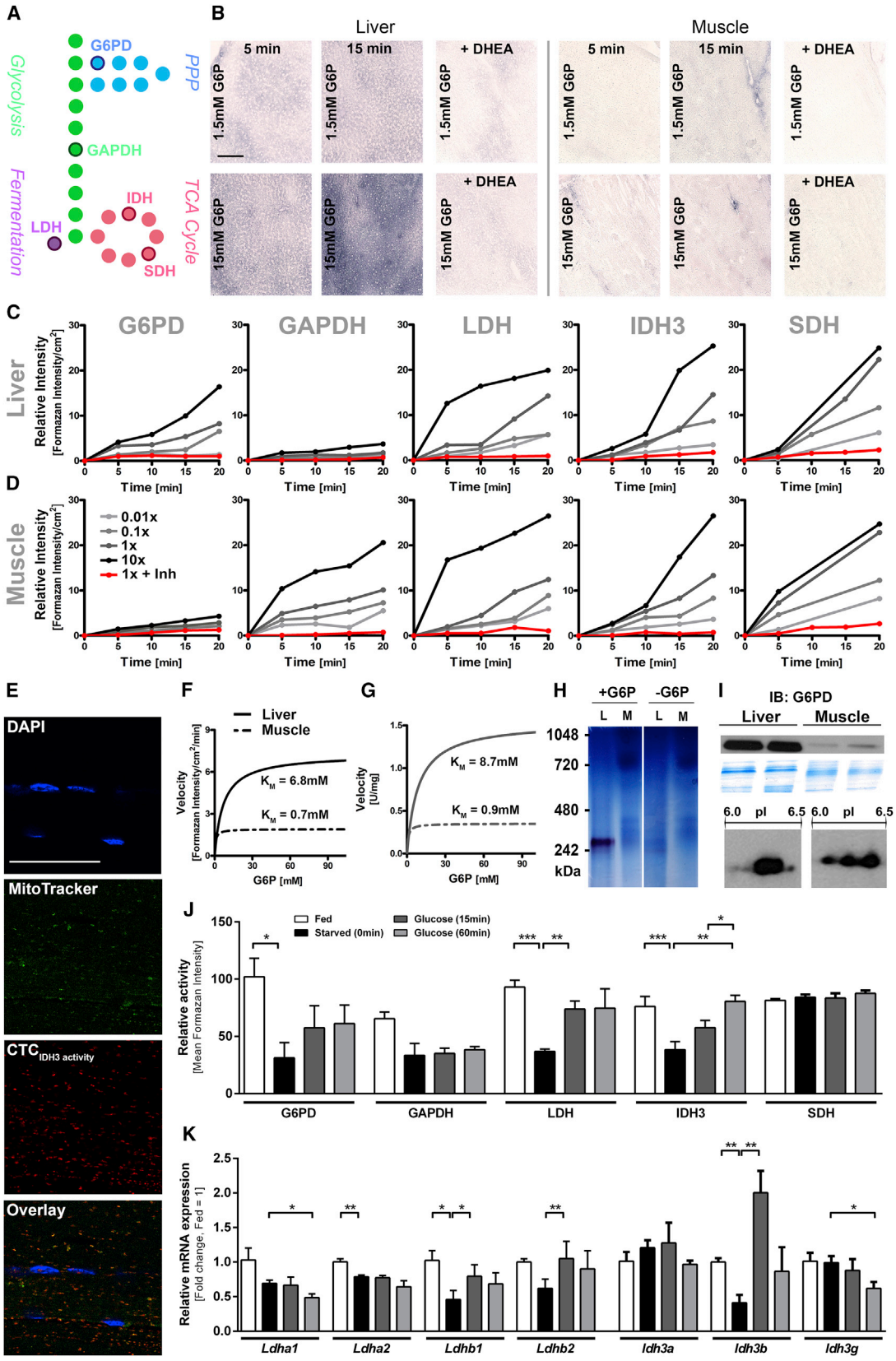

(legend on next page)

Thus, there is high demand for a method that allows identification and simultaneous metabolic characterization of single cells *in situ*. We here introduce a novel approach, which relies on enzyme histochemistry and automated whole-tissue histocytometry in order to combine information on enzymatic activities and cell marker expression. Technically, we perform enzyme activity assays and immunostain distinct cell types on consecutive tissue cryosections. Importantly, to determine the enzyme activities, we measure the amount of formed product over time (the initial velocity [V_0] or catalytic rate) at optimal and constant assay conditions, including saturating substrate and co-factor levels ($V_0 = V_{max}$). These measured activities can then be compared between samples and represent the amount of active enzyme in the analyzed samples (Bisswanger, 2014). Here, we provide activity data of up to five different dehydrogenases reflecting different metabolic pathways in single cells. The measured activities of the respective enzymes and their adaptations in response to physiological stimuli may serve as direct indicators for the configuration of the ''enzymatic backbone'' comprising the pathways of primary carbohydrate metabolism, including glycolysis, the pentose phosphate pathway (PPP), and the tricarboxylic acid (TCA) cycle. This powerful ensemble of complementary techniques allows us for the first time to analyze metabolic configurations of single cells in their intact microenvironment.

RESULTS

Enzyme Histochemistry Is a Valid Tool to Assess Enzymatic Activities *In Situ*

To assess the potential of our methodological concept, we first selected five metabolic enzymes that catalyze key reactions of cellular primary carbohydrate metabolism, including glucose-6-phosphate dehydrogenase (G6PD; PPP), glyceraldehyde 3-phosphate dehydrogenase (GAPDH; glycolysis), lactate dehydrogenase (LDH; fermentation), and mitochondrial isocitrate dehydrogenase 3 (IDH3; TCA cycle) as well as succinate dehydrogenase (SDH; TCA cycle) (Figure 1A). G6PD activity is a rate-limiting factor for glucose entering the oxidative PPP and therefore involved in nucleotide biosynthesis and in tuning cellular redox states (Ramos-Martinez, 2017; Stanton, 2012). GAPDH activity represents a central hub in glycolysis, can act as a rate-limiting step in aerobic glycolysis, and bridges metabolism and cell function (Chang et al., 2013; Colell et al., 2009; Schuppe-Koistinen et al., 1994; Shestov et al., 2014; Tristan et al., 2011). LDH activity reports us fermentation or aerobic glycolysis, and its activity is seen as hallmark feature of cancer (Doherty and Cleveland, 2013; Ganapathy-Kanniappan and Geschwind, 2013). IDH3 and SDH, two mitochondrial enzymes, have diverse functions beyond their roles in the Krebs cycle or the electron transport chain (SDH). Both enzymes appear to function at an interface of cellular metabolism, lipid synthesis, redox balance, and cell signaling events involved in oxygen sensing and link metabolism and cell function (Gaude and Frezza, 2014; Mills et al., 2016; Rutter et al., 2010; Zeng et al., 2015). The selected enzymes exert their catalytic activity at important nodes of glycolysis, PPP, and TCA cycle. All five enzymes are dehydrogenases, following the same detection principles, which are reliable and well documented in literature (Gomori, 1952; van Noorden and Frederiks, 1992). We next evaluated established enzyme histochemistry protocols for measuring the activities of these five enzymes (van Noorden and Frederiks, 1992). The assay principle is common for all selected enzymes and employs the colorless redox-sensitive tetrazolium salt nitroblue tetrazolium chloride (NBT) as a detection reagent. NBT can be directly reduced by NAD(P)H/H^+, the common reaction co-factor product of dehydrogenase activity, to its strongly colored mono- or diformazan state, which immediately binds to local proteins and thereby permits precise localization of the investigated enzymatic activity (Figure S1A). We also included an electron carrier to improve reaction efficiency and an inhibitor of the mitochondrial electron transport chain to block unspecific background signals in the activity assays. As negative controls, we used reactions containing no substrates and enzyme inhibitors at high concentrations for maximum inhibition, as previously reported (van Noorden and Frederiks, 1992).

In order to address specificity of the obtained signal, reproducibility of the NBT-based *in situ* activity assays, and validity of the approach to characterize distinct metabolic configurations, we tested the stainings of all five enzymatic activities in well-characterized and largely homogeneous mouse liver and muscle tissue, which are also known to have distinct metabolic configurations (Berg et al., 2002). To address specificity, we monitored the signal intensities obtained by increasing concentrations of the specific enzyme substrates on consecutive slides

Figure 1. Enzyme Histochemistry Is a Valid Tool to Assess Enzymatic Activities in Intact Tissues

(A) Schematic representation of the cellular primary carbohydrate metabolism indicating the five selected enzymes.

(B) Representative images of liver and muscle cryosections stained for the activity of G6PD using different concentrations of its substrate G6P. DHEA (Dehydroepiandrosterone) was used as negative control. Scale bar, 100 μm.

(C and D) The respective time and dose responses for all enzymes in liver (C) and muscle (D) tissue. Negative controls (no substrate) were used for background correction. The dose response was performed in decadic steps (for G6PD: x = 15 mM G6P, GAPDH: x = 2.5 mM G3P, LDH: x = 150 mM lactate, IDH3: x = 100 mM isocitrate, SDH: x = 60 mM succinate). Data represent the mean of at least three consecutive slides.

(E) Representative confocal microscopy pictures of muscle tissue stained with DAPI (blue), MitoTracker (green), and IDH3 activity (red) using CTC as detection reagent. Scale bar represents 50 μm.

(F) Michaelis-Menten kinetics of G6PD in liver and muscle cryosections obtained from the time- and dose-dependent activity stainings.

(G) Michaelis-Menten kinetics of G6PD activity in liver and muscle homogenates were measured by photometric detection of NADPH. Data represent the mean of three experiments.

(H and I) Representative images of an in-gel activity assay of G6PD (H) as well as 1D (I, top, Coomassie stain to indicate equal loading) and 2D (I, bottom) G6PD immunoblots.

(J and K) Activities of the indicated enzymes (J) and mRNA expression of LDH and IDH isoforms (K) in muscle tissue of mice fed *ad libitum* (fed), starved overnight (starved, 0 min), or re-fed with glucose for 15 or 60 min. Negative controls (inhibitors) were used for background correction in (J). Data represent mean of 3–4 mice and error bars indicate SEM.

(Figures 1B–1D; Figures S1B and S1C). Incubation of about 200 cryosections with the respective substrates and detection mixtures resulted in a time- and dose-dependent formazan formation for each enzyme (Figure 1B; Figure S1B). All reactions followed stoichiometric principles of enzyme kinetics and can therefore be used to define the respective enzyme activities for the tested reactions. Abrogation of the staining in both negative controls further confirmed the specificity of the obtained signals by the catalyzed reactions. Furthermore, co-localization of mitochondrial staining and IDH3 activity in muscle tissue, which we observed by confocal imaging, indicated that we can indeed monitor compartment- and isoform-specific enzyme activities (Figure 1E). For confocal imaging, we exchanged NBT with 5-Cyano-2,3-di-(p-tolyl)tetrazolium chloride (CTC) as a detection reagent and additionally co-stained mitochondria with MitoTracker. CTC, in contrast to NBT, emits a fluorescent signal upon reduction by $NAD(P)H/H^+$ (Frederiks et al., 2006) but is less stable than the NBT signal (data not shown) and was therefore only used for qualitative analysis and not for our primary quantitative approach.

In order to address reproducibility, we compared results obtained by the NBT-based activity assays with an alternative assay principle. We analyzed enzyme kinetics of G6PD in liver and muscle tissue side by side with an activity assay of crude protein tissue homogenates and direct photometric detection of NADPH (Figures 1F and 1G). Both approaches revealed comparable results, showing significantly higher K_M and V_{max} for liver G6PD compared to muscle G6PD. Comparing liver and muscle K_M and V_{max} values indicated qualitative and quantitative changes in G6PD. Kinetics analyses were also performed for GAPDH, LDH, IDH3, and SDH activities (Figure S1C). To further biochemically characterize the enzyme of interest and provide an explanation of observed qualitative and quantitative changes, we performed G6PD in-gel activity assays to assign a molecular weight to the responsible enzyme. Using NBT as detection reagent and G6P as substrate, we confirmed that the tetrameric form of liver G6PD (~240 kDa) showed enhanced enzymatic activity (Figure 1H). We also used 1D and 2D western blot analysis and could detect more G6PD protein in liver tissue samples than in muscle tissue and also an altered pattern of post-translational modifications (PTMs), which could be further characterized by mass spectrometry (Figure 1I).

To address validity of our approach and to demonstrate its utility to characterize metabolic configurations and reconfigurations, we measured metabolic changes in the same tissue across different physiological conditions. We measured enzymatic activities of all five enzymes at saturating substrate conditions to profile and compare tissue of fed (*ad libitum*) and fasted (overnight) mice and additionally demonstrated the metabolic response of fasted animals to orally administered glucose in a time-course experiment (fasted/0 min, 15 min, and 60 min). Thereby, we assessed changes in metabolic steady states (fed/fasted) and changes to a rapid and dynamic physiological response over time. For this experiment, we analyzed, in total, 150 slides (2 tissues × 5 enzymes × 15 animals), and each slide contained three consecutive tissue sections, one for the full reaction and two for negative control stainings. We presented the activity data as mean formazan intensity formed over time (15 min). Negative controls were used for background subtraction. This experiment revealed significant reconfiguration of the enzymatic machinery in response to these physiological stimuli in glucose consuming muscle tissue and only minor changes in glucose consuming and producing liver tissue (Figure 1J; Figure S1D). In muscle tissue of fasted mice, we observed a significant reduction of active G6PD, GAPDH, LDH, and IDH3, but not of SDH, compared to muscle tissue from fed animals. Feeding glucose to fasted animals resulted in a rapid recovery of measured G6PD, LDH, and IDH3 activities already after 15 min, though the extent and kinetics varied among the different enzymes. Measured GAPDH activities, while regulated upon fasting, as well as SDH activity, were not changed in response to glucose administration at the measured time points. We then further investigated in muscle tissue whether observed changes in LDH and IDH3 activities can be correlated to changes in mRNA expression levels of all seven relevant transcripts (Figure 1K). Active LDH is an isoenzyme and can consist of LDHA, LDHB, LDHC, and LDHD subunits encoded by four different genes, with *Ldha* and *Ldhb* each expressed as two distinct transcripts. In muscle tissue, we observed that *Ldha* and *Ldhb* transcripts levels were significantly reduced in the fasted animals when compared to the fed state. However, only *Ldhb* (*Ldhb1* and *Ldhb2* transcripts) appeared to be responsive to glucose administration. We did not detect *Ldhc* and *Ldhd* expression in muscle tissue. Active IDH3 is a heterotetramer encoded by three different genes (*Idh3a*, *Idh3b*, and *Idh3g*). Only *Idh3b* expression responded to fasting and to glucose. By comparing the enzyme activity data (Figure 1J) with actual gene expression (Figure 1K), we observed correlation of changes in *Ldhb* and *Idh3b* expression with changes in measured enzyme activities, as both responded to fasting and to glucose. However, looking at *Ldha* transcript levels, which is also known as the LDH muscle subunit forming the isoenzyme LDH5, we observed only a reduced expression by fasting, but no response to glucose administration, while measured LDH activity increased significantly. *Ldha1* and *Idh3g* gene expression was even found to inversely correlate with measured enzyme activity looking at 60 min after glucose administration. Comparing measured enzyme activities to mRNA and/or protein levels, including alternative transcript expression or PTMs, may reveal the potential mechanism of how cells adapt to reduce or to increase the amounts of active enzyme in response to a particular stimulus.

In summary, these results confirmed that NBT-based activity assays are specific, reproducible, and a valid tool to demonstrate and assess altered metabolic configurations in response to physiological stimuli *in situ*.

Enzyme Activities of Single Cells in Heterogeneous Tissues

In order to achieve a more detailed analysis of enzymatic activities in complex tissues, we made use of an automated histocytometry system to reach a single-cell resolution. Histocytometry platforms (also known as tissue cytometry or quantitative image cytometry) allow automatic acquisition and analysis of fluorescent and brightfield images of entire tissue sections (Gerner et al., 2012). Based on a nuclear staining, algorithms ultimately assign signal intensities from all channels to individual cells while retaining their spatial information (Figure S2) (Ecker and Steiner, 2004). In order to compare enzyme activities of cells between

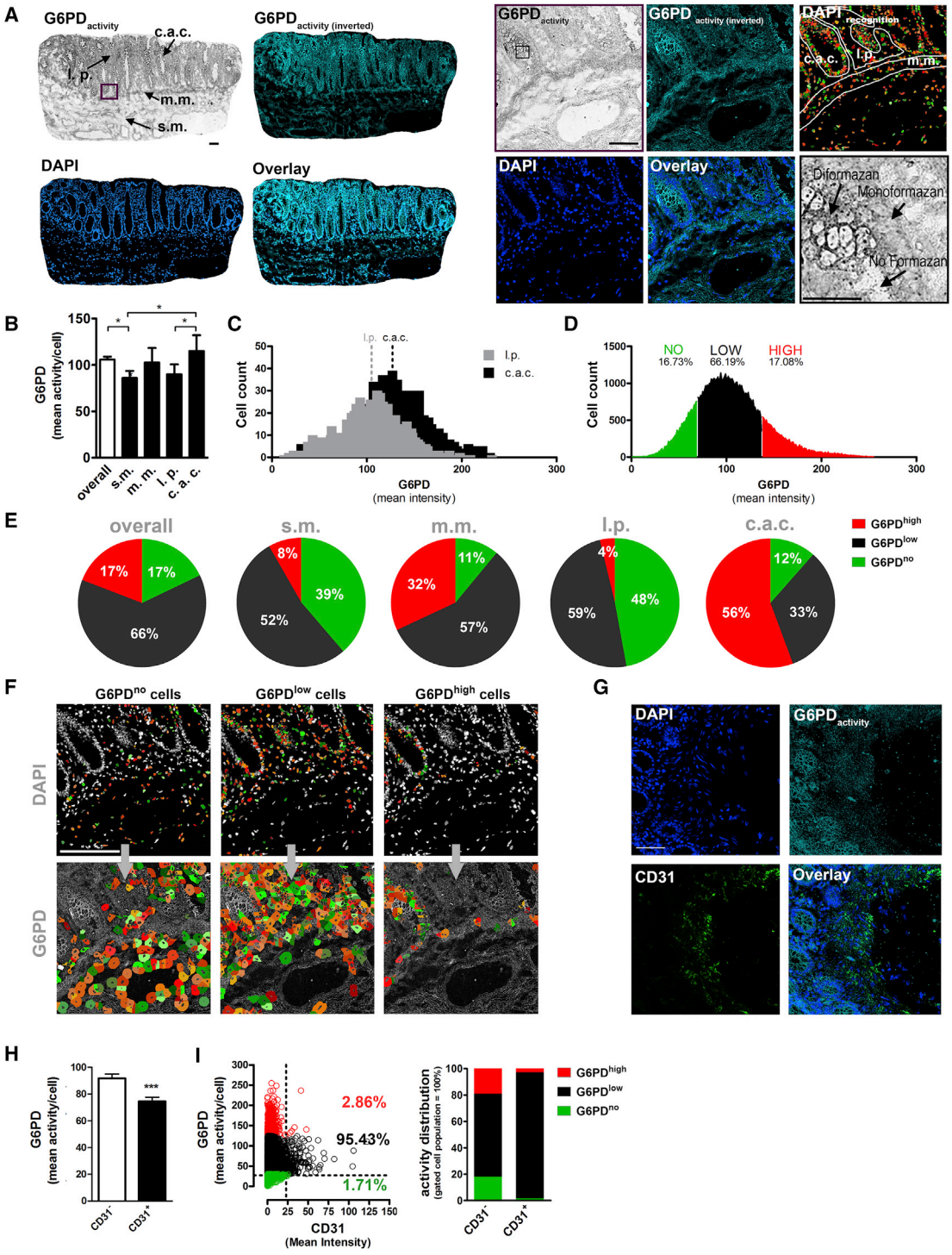

Figure 2. Enzymatic Activities of Single Cells in Complex Tissues

(A) Representative images of human colon tissue stained for the activity of G6PD and nuclear DAPI. Brightfield images were inverted, and on the basis of the nuclear staining, the colon tissue was segmented into the indicated morphological regions (see Results). Close ups of the indicated regions also indicate identified cells (colored dots) as well as no, mono-, and diformazan stainings (right). Scale bars represent 1 mm (section overview) and 100 μm (close ups).

(B) A bar graph representing the mean G6PD activity per cell of each indicated subregion. Error bars indicate SEM of four consecutive sections.

(C) Histogram to represent the distribution of mean G6PD activity for cells located in l.p. and c.a.c.

(D) Histogram to represent the distribution of mean G6PD activity for all cells and *no*, *low*, and *high* enzyme activity gates. The categorization was based on a negative control staining (*no* enzymatic activity) and on the formation of diformazan (*high* enzymatic activity).

(legend continued on next page)

different tissue compartments, we stained human colon tissue exemplarily for G6PD activity and co-stained the nuclear DNA of cells with DAPI (Figure 2A). The brightfield images, representing the enzymatic activities, were subsequently inverted to allow the combined analysis of brightfield and fluorescent images (Figure 2A). The compartments of the human colon tissue were grouped into submucosa (s.m.), muscularis mucosa (m.m.), lamina propia (l.p.), and columnar absorptive epithelial (c.a.c.) cells, and the mean G6DP activity (relative intensity/incubation time [R.I./time]) per cell for each region was compared to each other in a bar chart (Figure 2B). This analysis revealed that colon cells of this particular individual showed a significantly lower mean G6PD activity in s.m. and l.p. than cells in the c.a.c. compartment. The resulting data can also be represented in a histogram to provide information on the shape of activity distribution within a group of cells and the quantity of analyzed events (Figure 2C). In analogy to flow cytometry analysis, we also categorized the recognized cells in subgroups with "no," "low," or "high" enzymatic activities ($G6PD^{no}$, $G6PD^{low}$, and $G6PD^{high}$) to allow comparison of populations by frequency distribution analysis to the expense of resolution (Figure 2D). For our experiments, we defined $G6PD^{no}$, $G6PD^{low}$, and $G6PD^{high}$ cells by the respective negative control stainings (no-low cutoff) and the very intense precipitates of diformazan staining (low-high cutoff) (Figure 2A). Once defined, these cutoffs were kept constant. We applied these gates to our data and observed that around 17% of all recognized cells (n = 94,000 cells) had no detectable G6PD activity and were therefore gated as $G6PD^{no}$ cells, and about the same number of cells were $G6PD^{high}$ (Figure 2D). When analyzing the enzymatic activities between the different colon compartments, the distribution in the c.a.c. was shifted, and more than 50% of all cells were $G6PD^{high}$, while in the l.p. or s.m. compartment, $G6PD^{no}$ cells appeared over-represented (Figure 2E). Histocytometry provides the opportunity to relocate each cell in the original image ("backward gating") and thereby locally define the cells with distinct metabolic activities in the tissue. Backward gating visually confirmed that $G6PD^{high}$ cells were indeed primarily found in the c.a.c. compartment (Figure 2F).

In order to specifically assign enzymatic activities to particular cells, we combined the G6PD activity staining with immunofluorescence staining for the endothelial cell marker CD31 and DAPI in human colon tissue (Figure 2G). Histocytometry analysis of six consecutive cryosections revealed a mean G6PD activity per cell (R.I./time/cell) of 91.82 ± 3.13 SD for $CD31^-$ cells and 74.59 ± 2.94 SD for $CD31^+$ with an average cell count per section of 40,376 and 3,113, respectively (Figure 2H). The slide-to-slide consistency was assessed by the inter-assay coefficient of variability (% CV mean of 3.40 and 3.94 for $CD31^-$ and $CD31^+$ cells, respectively). The data were also presented by scatter blot analysis and frequency distribution analysis of cells categorized as $G6PD^{no}$, $G6PD^{low}$, and $G6PD^{high}$. This indicated that about 95% of the $CD31^+$ cells showed low G6PD activity and a relative homogeneous activity distribution within this cell type (Figure 2I). To this point, we managed to develop a reproducible imaging method, which allowed us to identify particular cell types and simultaneously characterize intracellular metabolic signatures in structurally intact human tissue at the single-cell level.

The Impact of a Tumor Environment on the Metabolic Phenotypes of Immune Cells

As proof of concept for our method, we aimed to profile the metabolic signatures of human T cell subsets and macrophage populations in healthy and cancerous human colon tissue microenvironments. As a test sample for this feasibility study, we obtained tumor tissue from one patient suffering from a tubular adenocarcinoma and matched healthy control tissue, which was removed about 10 cm from the tumor side. Immediately after surgical removal, the tissue was in part snap frozen in optimal cutting temperature (O.C.T.) media for metabolic imaging, and with the remaining tissue, we assessed the metabolic parameters oxygen consumption rates (OCRs) and extracellular acidification rates (ECAR) using the Seahorse XF analyzer. This analysis revealed that the tumorous tissue of this patient showed a 2-fold higher OCR and a 3-fold higher ECAR compared to healthy tissue (Figure 3A). The reduced OCR/ECAR ratio suggested a shift toward aerobic glycolysis, a phenomenon previously described as the Warburg effect (Vander Heiden et al., 2009) (Figure 3B).

To characterize the immune cell compartment of this specific patient, we used two different fluorescently labeled antibody sets, one to identify T cell subsets, including $CD8^+$, $CD4^+$, regulatory (Tregs; $CD4^+/FoxP3^+$), and T helper type 17 T cells (Th17; $CD4^+/CD161^+$), and one to identify macrophage populations ($MAC2^+/CD31^-$), which we further sub-gated into "non-inflamed" ($TNF\alpha^-/IL\text{-}6^-$), "inflamed" ($TNF\alpha^+/IL\text{-}6^+$), $TNF\alpha$, or IL-6 single-positive macrophages (Figures 3C–3F). To metabolically define this broad repertoire of immune cells in their intact microenvironment, we measured the activities of G6PD, GAPDH, LDH, IDH3, and SDH at saturating substrate conditions on consecutive sections and for each of the two antibody sets separately. By histocytometry, we detected around 6,000 cells/mm^2 tissue and analyzed an average of 6.5 mm^2 of tissue/section (Figure 3D). In the first step, we used the resulting scatter blots to gate for the different immune cells and revealed that this particular cancer patient displayed an inflamed phenotype, reflected by a significant increase in macrophages, $CD8^+$ cells, and Tregs and a significant decrease in $CD4^+$ T cells and Th17 cells (Figures 3G–3I; Figure S3). Additionally, we again color coded all cells according to no, low, or high enzymatic activity in order to visualize their relative distribution. For example, 90% of $G6PD^{no}$ macrophages in healthy tissue could be found in the $TNF\alpha^-/IL\text{-}6^+$ cells,

(E) Pie charts to demonstrate the distribution of cells with no, low, or high G6PD activity of each morphological subregion. Data represent the mean value of four consecutive slides.

(F) Representative images indicate identified cells (colored dots) with either no, low, or high activity in the original tissue via backward gating. Cells of each activity were highlighted in images of the nuclear DAPI staining (top) and images of G6PD activity stainings (bottom). Scale bar represents 100 μm.

(G) Representative images of colon tissue stained for G6PD activity, DAPI, and a fluorescently labeled CD31 antibody. Bar represents 100 μm.

(H) A bar graph representing the mean G6PD activity in $CD31^-$ and $CD31^+$ cells of six consecutive slides. Error bars indicate SEM.

(I) Representative scattergram and frequency distribution of $CD31^-$ and $CD31^+$ cells gated according to no, low, or high G6PD activity.

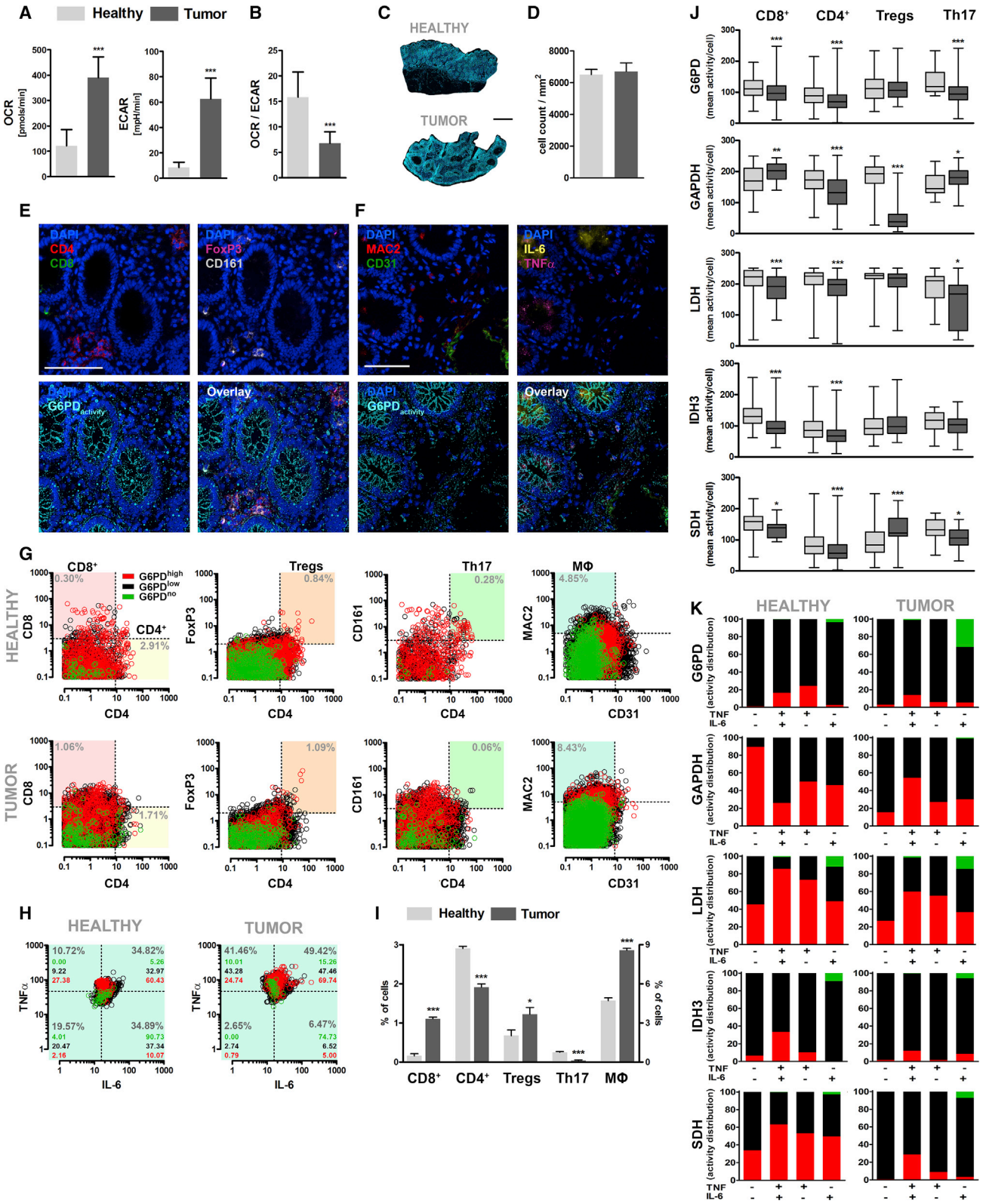

Figure 3. The Metabolic Configuration of Immune Cells within Healthy and Cancerous Colon Tissue

(A and B) ECAR and OCR recordings (A) of healthy and cancerous colon tissue from one patient to assess the respective OCR/ECAR ratio in (B) by the Seahorse XF Analyzer. Error bars represent the SD of ten replicates.

(legend continued on next page)

while G6PD^{high} cells were mainly found in TNFα^+/IL-6$^+$ and TNFα^+/IL-6$^-$ macrophage populations (Figure 3H).

Next, we compared the enzymatic signature of each cell population and assessed changes by comparing respective immune cells from healthy and tumor microenvironments. Exemplarily, we processed the raw data either by calculating the mean enzyme activity per cell for the different T cell subsets or by calculating the frequency distribution of no-, low-, and high-activity cells in macrophage populations, according to their inflammatory state (Figures 3J and 3K). The results of mean enzyme activities per cell were demonstrated in box plots to account for variations within populations, including skewness, dispersion, and outliers. Frequency distributions are a suitable form to summarize possible activity shifts of respective enzymes within sub-populations. Specifically, in CD4$^+$ and CD8$^+$ cells in the tumor, we measured reduced mitochondrial enzyme activities (IDH3 and SDH) accompanied by enhanced glycolytic GAPDH activity in CD8$^+$ and reduced aerobic glycolysis (GAPDH and LDH) in CD4$^+$ cells compared to respective cells in the healthy tissue. Furthermore, Tregs in the cancer microenvironment showed significantly less active glycolytic GAPDH and more active mitochondrial SDH compared to Tregs in the healthy tissue. Th17 cells in the cancer tissue showed reduced G6PD, LDH, and mitochondrial enzyme activities accompanied by an increase in measured GAPDH activity compared to Th17 cells in the healthy environment. Comparison of the enzyme activity profiles of normal tissue macrophages to tumor-associated macrophages (TAMs) revealed different metabolic configurations in inflamed and non-inflamed macrophages. TAMs generally had reduced enzymatic activities compared to the respective healthy tissue macrophages, and only inflamed TAMs showed an enlarged population with high GAPDH activity. Specifically, in the population of non-inflamed TAMs, less than 20% of the cells showed high GAPDH activity, while in normal tissue macrophages, more than 90% of all cells showed high GAPDH activity. Here, we report significant differences, which we specifically observed by comparing single cells (expressing the same marker proteins) found in healthy and tumor microenvironments. However, the specific environmental effects responsible for the observed changes in measured enzymes remained elusive and warrant further evaluations and functional testing. Together, these data suggest a significant impact of the microenvironment on the metabolic configurations of all analyzed immune cells.

The Metabolic Configuration of the Cellular Microenvironment in Human Breast Cancer

As a second example, we applied our method to investigate larger sample sizes and also to address higher-order complexity of cellular metabolism, namely *intercellular* metabolism of cancer-associated fibroblasts (CAFs) and cancer cells in their intact microenvironments. We used a commercially available breast cancer tissue array, which contained invasive ductal carcinoma biopsies of 35 patients with information on their estrogen receptor (ER), progesterone receptor (PR), and human epidermal growth factor receptor 2 (HER2) status. We obtained five consecutive slides of this tissue array and stained four for LDH, GAPDH, SDH, and G6PD activities at saturating substrate levels in combinations with fluorescently labeled antibodies against the proliferation marker ki67 and the CAF marker FAP (fibroblast activation protein) and DAPI for single-cell recognition (Figures 4A–4C). In addition to antibody-based cell identification, we used the remaining consecutive slide for hematoxylin and eosin (H&E) staining to identify the tumor bulk as morphological compartment (Figure 4D).

We first calculated the mean enzyme activities per cell for all cellular compartments and visualized their individual LDH, G6PD, GAPDH, and SDH activities in scatter dot plots. Each dot represents one patient's mean activity of all identified cells within those compartments. This analysis revealed that in this cohort, CAFs displayed significantly higher activities in all measured enzymes, indicating enhanced metabolic activity compared to cells of the solid tumor mass and the ki67$^+$ cells (Figure 4E). However, the proliferating ki67$^+$ cells showed significantly enhanced G6PD activity as compared to the tumor bulk. To test whether cells of ER/PR, HER2, or triple-negative cancer subgroups possess specific metabolic configurations, we exemplarily compared LDH activity, a hallmark of cancer metabolism, within the tumor bulk and observed that cells of ER/PR tumors had significantly lower mean LDH activity than HER2 or triple-negative tumors (Figure 4F). A heatmap analysis containing the entire dataset again indicated that the highest metabolic activity was found in FAP$^+$ cells, but clustering of patient subgroups did not reveal any obvious additional metabolic patterns (Figure 4G).

To investigate a possibly conserved intercellular LDH activity pattern between cancer cell subsets and CAFs, we used the intracellular LDH activity data and a two-step correlation analysis (Figure 4H). We first calculated pairwise Pearson correlation coefficients between all cellular compartments and then

(C) Representative whole-tissue images from this patient. Scale bar represents 1 mm.

(D) Analysis by histocytometry revealed a similar cell count per mm^2 in both tissues (healthy, light bars; tumor, dark bars). Error bars represent the SEM of five consecutive slides.

(E) Representative images of activity stainings combined with fluorescently labeled antibody stainings for CD4, CD8, FoxP3, and CD161. Scale bar represents 100 μm.

(F) Representative images of activity stainings combined with fluorescently labeled antibody stainings for MAC2, CD31, IL-6, and TNFα. Scale bar represents 100 μm.

(G) Scattergrams indicating the relative distribution of individual cell types in healthy and tumor tissue. Each cell was color coded for no (green), low (black), or high (red) G6PD activity, respectively.

(H) Sub-gating of MAC2$^+$ CD31$^-$ cells for TNFα and IL-6, and each cell was again color coded for G6PD activity gates. The percentages in the respective graphs refer to the whole population.

(I) Bar graph comparing the relative distribution of T cells and macrophages in healthy and tumor tissue. Left y axis refers to T cells, and the right y axis refers to macrophages (Mϕ). Error bars represent the SEM of five consecutive slides.

(J) Boxplot with whiskers (min to max) of respective enzymatic activity in different T cell populations in healthy (light bar) and tumor tissue (dark bar).

(K) Frequency distribution of the respective enzymatic activities in macrophage subpopulations in healthy and tumor tissue.

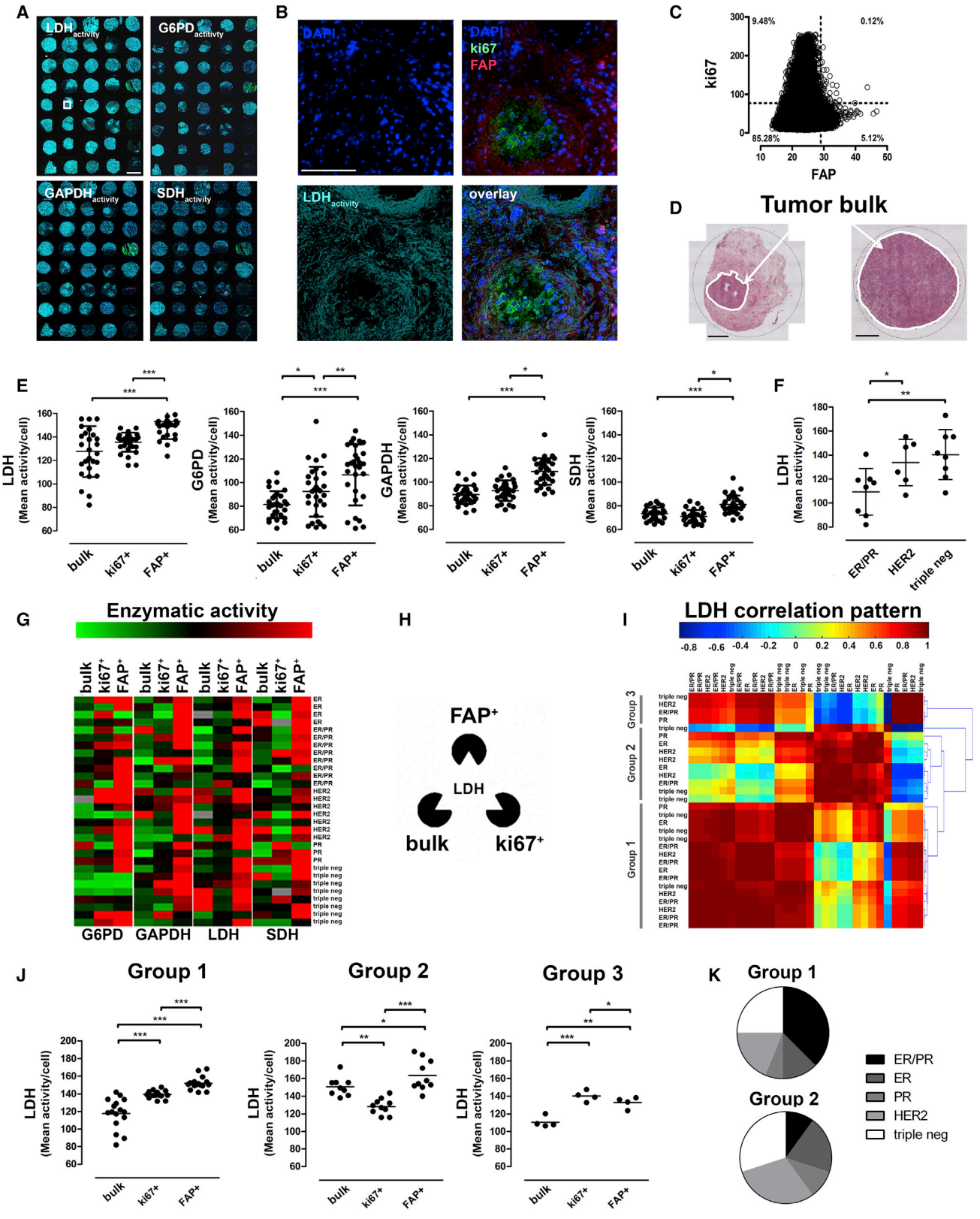

Figure 4. The Metabolic Configuration in Human Breast Cancer Microenvironments

(A) Consecutive slides of a breast cancer tissue microarray were stained for the activities of the indicated enzymes together with fluorescently labeled antibodies against the proliferation marker ki67 and the activated fibroblast marker FAP. Scale bar, 2 mm.

(legend continued on next page)

correlated all patients in a resulting 30 × 30 correlation matrix (Figure 4I). A hierarchical cluster tree based on the highest correlations within the matrix was built to identify patient subgroups with a specific intercellular LDH correlation pattern. This resulted in the identification of three unique and metabolically defined ductal carcinoma patient subgroups. To visualize their respective intercellular LDH activity configurations, we compared the mean LDH activity per cell of each cell type in the tumor microenvironment for each group individually (Figure 4J). Two groups (1 and 2) showed the highest LDH activity in FAP^+ cells; however, group 1 had higher LDH activity in the $ki67^+$ proliferating cells than cells in the tumor bulk, while group 2 showed an opposite metabolic configuration (significantly higher LDH activity in the tumor bulk cells than in $ki67^+$ cells). The third group, although only representing a few cases, displayed the highest LDH activity in $ki67^+$ cells followed by FAP^+ cells and cells of the tumor bulk. Taking the available information of the ER, PR, and HER2 status into account and comparing these metabolic groups to the intrinsic breast cancer subtypes revealed that, specifically, the ER and PR double-positive cancer subtypes enriched in the first group (six out of eight analyzed biopsies were found in group 1, one in group 2, and one in group 3; Figure 4K). This indicated to us that intrinsic subtypes of breast cancer are, per se, not restricted to one of our identified groups and that some subtypes appear to have preferential metabolic configurations. A representative sample size and further careful clinical evaluations of such metabolically defined patient subgroups are required to reveal whether they are of prognostic or predictive value as novel and dynamic biomarkers.

DISCUSSION

In addition to sustaining bioenergetic demands, metabolic pathways also represent central hubs with significant impact on complex signaling networks, which modulate cell function. The loss of the physical interaction of p53 with G6PD by tumor-associated mutations in p53, as well as the binding of GAPDH as an RNA-binding protein to interferon gamma mRNA in T cells are just two prominent examples for these cross-talks (Chang et al., 2013; Jiang et al., 2011). However, most of the previous work either assumed homogeneity of the tissue samples or assessed metabolic states of isolated cell populations *in vitro*. Loss of tissue integrity by cell isolation procedures may alter the metabolic configuration of cells, as metabolism is a highly dynamic process and extremely sensitive to external stimuli. The metabolic imaging method presented here allows reproducible and sensitive measurement of enzymatic activities in distinct cells at the single-cell level in their intact microenvironments.

Despite the methodological progress of our method, this technique also has its limitations, which are mainly based on the employed tools: enzyme histochemistry (including enzyme activity assays) and histocytometry (including immunofluorescence). Increasing the number of markers on single slides will provide a more detailed characterization of cells and can be achieved by, for example, employing various commercial multiplexing platforms or even more sophisticated approaches like tissue mass cytometry (Giesen et al., 2014). A great advantage of enzymes is that they can be identified and quantified specifically by their catalyzed reaction. However, enzyme activity assays cannot be conducted *ex vivo* under physiological conditions and only provide information for the tested catalyzed reaction, indicating the limits of this approach and interpretation of its results. *In vivo*, enzymatic activity is not only defined by the amount of active enzyme, it is multi-factorial and co-defined by bioavailability of substrates and diverse co-factors as well as all other modulators of activity such as feedback loops triggered by, for example, allosteric regulation (Berg et al., 2002). Additionally, many enzymes use multiple substrates and also operate in two directions. If conducted properly, activity assays can reveal unique features of metabolic regulation at the enzyme level; however, this information does not allow any valid conclusions related to the actual metabolic flux *in vivo*. Despite these limitations, enzyme histochemistry represents a large toolbox with diverse possibilities of application, which allows us to assess the adaptations of various enzymatic activities, including transferases (for instance kinases), hydrolases, and lyases (van Noorden and Frederiks, 1992). We see emerging MALDI imaging techniques as powerful complementary tools to quantify small molecules *in situ* in order to additionally provide spatial information on substrate bioavailability (Fujimura and Miura, 2014; Miyazawa et al., 2017; Schwamborn et al., 2017).

Cancer biology and immunometabolism served us as prime examples to demonstrate the importance of spatially resolved information on cellular metabolism in complex tissue. Immune cell activation and subsequent phenotypic adaptation into different effector states are characterized by distinct metabolic patterns. Blocking glycolysis or inhibiting glucose uptake during T cell activation has been shown to alleviate their activation, T helper cell differentiation, and production of effector cytokines (Chang and Pearce, 2016; Palmer et al., 2015; Pearce and Pearce, 2013). In macrophages, reduction of mitochondrial metabolism after activation is essential to enable a pro-inflammatory immune response, accompanied by increased oxidation of succinate by SDH to enable reactive oxygen species production (Mills et al., 2016). Additionally, recent reports even indicate that nutrient competition in the tumor microenvironment can

(B) Representative close-up image of one breast cancer specimen stained for the activity of LDH, DAPI, ki67, and FAP. Scale bar, 100 μm.
(C) Representative scattergram to indicate gating strategy for the indicated cell populations.
(D) Two representative H&E stainings of the solid tumor bulk. Scale bar, 500 μm.
(E) In all ductal carcinoma patients, the mean activities of the indicated enzymes were analyzed within the cells of the different compartments. Error bars indicate the SEM.
(F) Exemplarily, the mean LDH activity in cells of the tumor bulk was grouped and compared according to the indicated classification. Error bars indicate the SEM.
(G) Heatmap of all measured mean enzyme activities in cells of the tumor bulk, $ki67^+$, and FAP^+ cells.
(H) A schema to illustrate the intercellular LDH activity between the indicated cell types.
(I) Pairwise correlation analysis and hierarchical clustering of the intercellular LDH activity between the tumor bulk, $ki67^+$, and FAP^+ cells.
(J) LDH activity in the different cell types in the metabolically defined patient subgroups with similar intercellular LDH activity.
(K) Distribution of intrinsic cancer subtypes within the metabolically defined breast cancer groups 1 (n = 16) and 2 (n = 10).

directly dampen immune cell effector functions (Chang et al., 2015). In line with the literature, we also observed an enhanced presence of $CD8^+$ T cells and inflammatory macrophages accompanied by metabolic configurations of the $CD4^+$, Th17, and especially Tregs that indicate the manifestation of an immunosuppressive microenvironment in the tumor of this particular patient (Chang et al., 2015; Ho et al., 2015). Recent advances in different strategies of cancer immunotherapy, including checkpoint blockades, adoptive T cell transfer (ACT), and chimeric-antigen receptor T cells (CARs), raise questions about how the tumor microenvironment inhibits immune cell function and how this might be overcome (Srivastava and Riddell, 2015).

In this study, we also addressed a lively discussed topic in cancer biology, namely intercellular metabolism. Certain metabolic relationships, for example, between oxidative and glycolytic cancer cells or between CAFs and cancer cells, have been found to impact tumor growth, metastatic potential, patient survival, and even treatment success (Koukourakis et al., 2006; Martinez-Outschoorn et al., 2011; Slany et al., 2015; Sonveaux et al., 2008). Tools to assess such complex biological systems are mainly based on co-culturing cells or mouse models employing cell-type-specific gene targeting. We have identified conserved intercellular patterns by correlating intracellular LDH activities of cancer and stromal cells, which appear to be preferentially employed by ER^+/PR^+ intrinsic subtypes of breast cancers. This raises two important questions: does treatment/drug efficiency of certain intrinsic breast cancer subtypes maybe depend on their metabolic fingerprint, i.e., does triple-negative cancer of group 1 and group 2 show the same prognosis or does it respond differently to various anti-cancer treatment regimens? Do these metabolic patterns reflect different stages of tumorigenesis? Additionally, we observed that CAFs had higher activities of all measured enzymes compared to the cancerous cells, irrespective of their proliferative potential (ki67 status). These data appear to be in line with the "reverse Warburg effect," which postulates that certain types of epithelial breast cancer cells can induce aerobic glycolysis in surrounding CAFs. In this model, CAFs secrete glycolytic intermediates, such as lactate, which can then be directly taken up by cancer cells to fuel their oxidative mitochondrial metabolism and enhance their proliferative potential (Migneco et al., 2010; Pavlides et al., 2009; Witkiewicz et al., 2012). The activity of a single enzyme does not define an entire metabolic pathway or the actual flux of, for example, lactate, but enzyme activity data can provide an additional and crucial layer of information to understand intercellular metabolic relationships within native tissue environments. To assess the complex CAF-cancer cell symbiosis *in situ*, it would be crucial to, in addition to LDH activities, (at least) (1) determine the expression of different monocarboxylate transporters as additional markers (indicating import and export of lactate), (2) also measure the activities of pyruvate dehydrogenase and other TCA enzymes (indicating intracellular lactate metabolism) in single cells, and (3) preferentially quantify intra- and extracellular ^{13}C-labeled lactate and pyruvate levels formed after a short pulse of ^{13}C-glucose administered *in vivo*. This *in situ* assessment, together with functional testing of the system (i.e. by gain- and loss-of-function models), would eventually disclose the *in vivo* nature of lactate shuttling between CAFs and breast cancer cells within their native environment. We need to consider the concepts of metabolic control, including coarse and fine control, and intrinsic and extrinsic regulation of metabolism to understand such complex systems in more detail.

An important goal for future studies is to better understand and define the metabolic configurations of all microenvironmental inhabitants, including tumor cells, infiltrating immune cells, as well as resident stromal cells, and to establish how their metabolic configurations may reflect or even predict the potential success to a certain therapeutic regime (Alizadeh et al., 2015). We believe that data on intercellular metabolic relationships will aid precision medicine approaches by revealing further mechanistic features of tumor, stroma, and immune cells, which can be targeted. Taken together, we presented a metabolic imaging method to assess the enzymatic configuration of single cells within their intact tissue microenvironment. We envision multiple application scenarios for this method and experience it as a new powerful and complementary tool to investigate cellular metabolism also *in situ*.

STAR★METHODS

Detailed methods are provided in the online version of this paper and include the following:

- KEY RESOURCES TABLE
- CONTACT FOR REAGENT AND RESOURCE SHARING
- EXPERIMENTAL MODEL AND SUBJECT DETAILS
  - Tissue Samples
  - Breast Cancer Tissue Array
- METHOD DETAILS
  - Metabolic Imaging
  - Confocal Laser Scanning Microscopy
  - Western Blots
  - G6PD In-Gel Activity Assay
  - G6PD Activity Assay in Tissue Homogenates
  - RNA Isolation, cDNA Synthesis, and Real-Time Quantitative PCR
  - Cellular Respiration and Extracellular Acidification
- QUANTIFICATION AND STATISTICAL ANALYSIS
  - Heatmaps and Correlation Analysis
  - Statistical Analysis

SUPPLEMENTAL INFORMATION

Supplemental Information includes three figures and can be found with this article online at http://dx.doi.org/10.1016/j.cmet.2017.08.014.

AUTHOR CONTRIBUTIONS

The study was conceived by A.M. and A.H. The research was carried out by A.M., C.N., J.L., E.P., and P.S. B.K. performed bioinformatic data processing, and M.G. assisted in the technological development. A.H., A.M., M.B., and O.W. contributed to the study design. Resources were provided by A.H., M.B., and O.W. A.H., A.M., and P.S. wrote the original draft of the manuscript. All of the authors reviewed and edited the manuscript. The study was supervised by A.H.

ACKNOWLEDGMENTS

We are grateful to Karin Hagenbichler, Stephan Miller, Sabine Rauscher, Balazs Hegedus, Tobias Müller, Thomas Weichhart, Rodrig Marculescu, Mate Kiss, Nikolina Papac-Milicevic, Martin Bilban, and Christoph Binder for

their support. This study was supported by department funds from the Department of Laboratory Medicine, Medical University of Vienna.

Received: February 6, 2017
Revised: May 26, 2017
Accepted: August 11, 2017
Published: September 7, 2017

REFERENCES

Alizadeh, A.A., Aranda, V., Bardelli, A., Blanpain, C., Bock, C., Borowski, C., Caldas, C., Califano, A., Doherty, M., Elsner, M., et al. (2015). Toward understanding and exploiting tumor heterogeneity. Nat. Med. *21*, 846–853.

Berg, J.M., Tymoczko, J.L., and Stryer, L. (2002). Biochemistry, Fifth Edition (W.H. Freeman).

Bisswanger, H. (2014). Enzyme assays. Perspect. Sci. *1*, 41–55.

Cairns, R.A., Harris, I.S., and Mak, T.W. (2011). Regulation of cancer cell metabolism. Nat. Rev. Cancer *11*, 85–95.

Chang, C.H., and Pearce, E.L. (2016). Emerging concepts of T cell metabolism as a target of immunotherapy. Nat. Immunol. *17*, 364–368.

Chang, C.H., Curtis, J.D., Maggi, L.B., Jr., Faubert, B., Villarino, A.V., O'Sullivan, D., Huang, S.C., van der Windt, G.J., Blagih, J., Qiu, J., et al. (2013). Posttranscriptional control of T cell effector function by aerobic glycolysis. Cell *153*, 1239–1251.

Chang, C.H., Qiu, J., O'Sullivan, D., Buck, M.D., Noguchi, T., Curtis, J.D., Chen, Q., Gindin, M., Gubin, M.M., van der Windt, G.J., et al. (2015). Metabolic competition in the tumor microenvironment is a driver of cancer progression. Cell *162*, 1229–1241.

Colell, A., Green, D.R., and Ricci, J.E. (2009). Novel roles for GAPDH in cell death and carcinogenesis. Cell Death Differ. *16*, 1573–1581.

Doherty, J.R., and Cleveland, J.L. (2013). Targeting lactate metabolism for cancer therapeutics. J. Clin. Invest. *123*, 3685–3692.

Ecker, R.C., and Steiner, G.E. (2004). Microscopy-based multicolor tissue cytometry at the single-cell level. Cytometry A *59*, 182–190.

Frederiks, W.M., van Marle, J., van Oven, C., Comin-Anduix, B., and Cascante, M. (2006). Improved localization of glucose-6-phosphate dehydrogenase activity in cells with 5-cyano-2,3-ditolyl-tetrazolium chloride as fluorescent redox dye reveals its cell cycle-dependent regulation. J. Histochem. Cytochem. *54*, 47–52.

Fridman, W.H., Pagès, F., Sautès-Fridman, C., and Galon, J. (2012). The immune contexture in human tumours: impact on clinical outcome. Nat. Rev. Cancer *12*, 298–306.

Fujimura, Y., and Miura, D. (2014). MALDI mass spectrometry imaging for visualizing in situ metabolism of endogenous metabolites and dietary phytochemicals. Metabolites *4*, 319–346.

Gajewski, T.F., Schreiber, H., and Fu, Y.X. (2013). Innate and adaptive immune cells in the tumor microenvironment. Nat. Immunol. *14*, 1014–1022.

Ganapathy-Kanniappan, S., and Geschwind, J.F. (2013). Tumor glycolysis as a target for cancer therapy: progress and prospects. Mol. Cancer *12*, 152.

Gascard, P., and Tlsty, T.D. (2016). Carcinoma-associated fibroblasts: orchestrating the composition of malignancy. Genes Dev. *30*, 1002–1019.

Gaude, E., and Frezza, C. (2014). Defects in mitochondrial metabolism and cancer. Cancer Metab. *2*, 10.

Gerner, M.Y., Kastenmuller, W., Ifrim, I., Kabat, J., and Germain, R.N. (2012). Histo-cytometry: a method for highly multiplex quantitative tissue imaging analysis applied to dendritic cell subset microanatomy in lymph nodes. Immunity *37*, 364–376.

Ghesquière, B., Wong, B.W., Kuchnio, A., and Carmeliet, P. (2014). Metabolism of stromal and immune cells in health and disease. Nature *511*, 167–176.

Giesen, C., Wang, H.A., Schapiro, D., Zivanovic, N., Jacobs, A., Hattendorf, B., Schüffler, P.J., Grolimund, D., Buhmann, J.M., Brandt, S., et al. (2014). Highly multiplexed imaging of tumor tissues with subcellular resolution by mass cytometry. Nat. Methods *11*, 417–422.

Glock, G.E., and McLean, P. (1953). Further studies on the properties and assay of glucose 6-phosphate dehydrogenase and 6-phosphogluconate dehydrogenase of rat liver. Biochem. J. *55*, 400–408.

Gomori, G. (1952). Histochemistry of enzymes. J. Mt. Sinai Hosp. N. Y. *19*, 446–451.

Hanahan, D., and Weinberg, R.A. (2011). Hallmarks of cancer: the next generation. Cell *144*, 646–674.

Ho, P.C., Bihuniak, J.D., Macintyre, A.N., Staron, M., Liu, X., Amezquita, R., Tsui, Y.C., Cui, G., Micevic, G., Perales, J.C., et al. (2015). Phosphoenolpyruvate is a metabolic checkpoint of anti-tumor T cell responses. Cell *162*, 1217–1228.

Jiang, P., Du, W., Wang, X., Mancuso, A., Gao, X., Wu, M., and Yang, X. (2011). p53 regulates biosynthesis through direct inactivation of glucose-6-phosphate dehydrogenase. Nat. Cell Biol. *13*, 310–316.

Kalluri, R. (2016). The biology and function of fibroblasts in cancer. Nat. Rev. Cancer *16*, 582–598.

Kamphorst, J.J., and Gottlieb, E. (2016). Cancer metabolism: friendly neighbours feed tumour cells. Nature *536*, 401–402.

Koukourakis, M.I., Giatromanolaki, A., Harris, A.L., and Sivridis, E. (2006). Comparison of metabolic pathways between cancer cells and stromal cells in colorectal carcinomas: a metabolic survival role for tumor-associated stroma. Cancer Res. *66*, 632–637.

Loftus, R.M., and Finlay, D.K. (2016). Immunometabolism: cellular metabolism turns immune regulator. J. Biol. Chem. *291*, 1–10.

Martinez-Outschoorn, U.E., Goldberg, A., Lin, Z., Ko, Y.H., Flomenberg, N., Wang, C., Pavlides, S., Pestell, R.G., Howell, A., Sotgia, F., and Lisanti, M.P. (2011). Anti-estrogen resistance in breast cancer is induced by the tumor microenvironment and can be overcome by inhibiting mitochondrial function in epithelial cancer cells. Cancer Biol. Ther. *12*, 924–938.

Migneco, G., Whitaker-Menezes, D., Chiavarina, B., Castello-Cros, R., Pavlides, S., Pestell, R.G., Fatatis, A., Flomenberg, N., Tsirigos, A., Howell, A., et al. (2010). Glycolytic cancer associated fibroblasts promote breast cancer tumor growth, without a measurable increase in angiogenesis: evidence for stromal-epithelial metabolic coupling. Cell Cycle *9*, 2412–2422.

Mills, E.L., Kelly, B., Logan, A., Costa, A.S., Varma, M., Bryant, C.E., Tourlomousis, P., Däbritz, J.H., Gottlieb, E., Latorre, I., et al. (2016). Succinate dehydrogenase supports metabolic repurposing of mitochondria to drive inflammatory macrophages. Cell *167*, 457–470.e13.

Miyazawa, H., Yamaguchi, Y., Sugiura, Y., Honda, K., Kondo, K., Matsuda, F., Yamamoto, T., Suematsu, M., and Miura, M. (2017). Rewiring of embryonic glucose metabolism via suppression of PFK-1 and aldolase during mouse chorioallantoic branching. Development *144*, 63–73.

Motz, G.T., and Coukos, G. (2013). Deciphering and reversing tumor immune suppression. Immunity *39*, 61–73.

Nakazawa, M.S., Keith, B., and Simon, M.C. (2016). Oxygen availability and metabolic adaptations. Nat. Rev. Cancer *16*, 663–673.

Ninfali, P., Aluigi, G., and Pompella, A. (1997). Methods for studying the glucose-6-phosphate dehydrogenase activity in brain areas. Brain Res. Brain Res. Protoc. *1*, 357–363.

O'Neill, L.A., and Pearce, E.J. (2016). Immunometabolism governs dendritic cell and macrophage function. J. Exp. Med. *213*, 15–23.

O'Neill, L.A., Kishton, R.J., and Rathmell, J. (2016). A guide to immunometabolism for immunologists. Nat. Rev. Immunol. *16*, 553–565.

Palmer, C.S., Ostrowski, M., Balderson, B., Christian, N., and Crowe, S.M. (2015). Glucose metabolism regulates T cell activation, differentiation, and functions. Front. Immunol. *6*, 1.

Pavlides, S., Whitaker-Menezes, D., Castello-Cros, R., Flomenberg, N., Witkiewicz, A.K., Frank, P.G., Casimiro, M.C., Wang, C., Fortina, P., Addya, S., et al. (2009). The reverse Warburg effect: aerobic glycolysis in cancer associated fibroblasts and the tumor stroma. Cell Cycle *8*, 3984–4001.

Pearce, E.L., and Pearce, E.J. (2013). Metabolic pathways in immune cell activation and quiescence. Immunity *38*, 633–643.

Ramos-Martinez, J.I. (2017). The regulation of the pentose phosphate pathway: remember Krebs. Arch. Biochem. Biophys. *614*, 50–52.

Rutter, J., Winge, D.R., and Schiffman, J.D. (2010). Succinate dehydrogenase—assembly, regulation and role in human disease. Mitochondrion *10*, 393–401.

Schuppe-Koistinen, I., Moldéus, P., Bergman, T., and Cotgreave, I.A. (1994). S-thiolation of human endothelial cell glyceraldehyde-3-phosphate dehydrogenase after hydrogen peroxide treatment. Eur. J. Biochem. *221*, 1033–1037.

Schwamborn, K., Kriegsmann, M., and Weichert, W. (2017). MALDI imaging mass spectrometry—from bench to bedside. Biochim. Biophys. Acta *1865*, 776–783.

Shestov, A.A., Liu, X., Ser, Z., Cluntun, A.A., Hung, Y.P., Huang, L., Kim, D., Le, A., Yellen, G., Albeck, J.G., and Locasale, J.W. (2014). Quantitative determinants of aerobic glycolysis identify flux through the enzyme GAPDH as a limiting step. eLife *3*, 3.

Slany, A., Bileck, A., Muqaku, B., and Gerner, C. (2015). Targeting breast cancer-associated fibroblasts to improve anti-cancer therapy. Breast *24*, 532–538.

Sonveaux, P., Végran, F., Schroeder, T., Wergin, M.C., Verrax, J., Rabbani, Z.N., De Saedeleer, C.J., Kennedy, K.M., Diepart, C., Jordan, B.F., et al. (2008). Targeting lactate-fueled respiration selectively kills hypoxic tumor cells in mice. J. Clin. Invest. *118*, 3930–3942.

Srivastava, S., and Riddell, S.R. (2015). Engineering CAR-T cells: design concepts. Trends Immunol. *36*, 494–502.

Stanton, R.C. (2012). Glucose-6-phosphate dehydrogenase, NADPH, and cell survival. IUBMB Life *64*, 362–369.

TeSlaa, T., and Teitell, M.A. (2014). Techniques to monitor glycolysis. Methods Enzymol. *542*, 91–114.

Tristan, C., Shahani, N., Sedlak, T.W., and Sawa, A. (2011). The diverse functions of GAPDH: views from different subcellular compartments. Cell. Signal. *23*, 317–323.

Turley, S.J., Cremasco, V., and Astarita, J.L. (2015). Immunological hallmarks of stromal cells in the tumour microenvironment. Nat. Rev. Immunol. *15*, 669–682.

Van den Bossche, J., O'Neill, L.A., and Menon, D. (2017). Macrophage immunometabolism: where are we (going)? Trends Immunol. *38*, 395–406.

van Noorden, C.J.F., and Frederiks, W.M. (1992). Enzyme Histochemistry: A Laboratory Manual of Current Methods (Oxford University Press/Royal Microscopical Society).

Vander Heiden, M.G., Cantley, L.C., and Thompson, C.B. (2009). Understanding the Warburg effect: the metabolic requirements of cell proliferation. Science *324*, 1029–1033.

Witkiewicz, A.K., Whitaker-Menezes, D., Dasgupta, A., Philp, N.J., Lin, Z., Gandara, R., Sneddon, S., Martinez-Outschoorn, U.E., Sotgia, F., and Lisanti, M.P. (2012). Using the "reverse Warburg effect" to identify high-risk breast cancer patients: stromal MCT4 predicts poor clinical outcome in triple-negative breast cancers. Cell Cycle *11*, 1108–1117.

Zeng, L., Morinibu, A., Kobayashi, M., Zhu, Y., Wang, X., Goto, Y., Yeom, C.J., Zhao, T., Hirota, K., Shinomiya, K., et al. (2015). Aberrant IDH3α expression promotes malignant tumor growth by inducing HIF-1-mediated metabolic reprogramming and angiogenesis. Oncogene *34*, 4758–4766.

STAR★METHODS

KEY RESOURCES TABLE

REAGENT or RESOURCE	SOURCE	IDENTIFIER
Antibodies		
APC Mouse anti-human CD161 (clone DX12)	BD Bioscience	Cat#550968, RRID: AB_398482
Alexa 700 Mouse anti-human CD8 (clone RPA-T8)	BD Bioscience	Cat#557945, RRID: AB_396953
PE-CF594 Rat anti-human IL-6 (Clone MQ2-13A5)	BD Bioscience	Cat#563543
FITC Mouse anti-human Ki-67 (Clone 35)	BD Bioscience	Cat#612472, RRID: AB_399649
Alexa 700 Mouse anti-human TNF (Clone Mab11)	BD Bioscience	Cat#557996, RRID: AB_396978
Alexa 488 Rabbit anti-human CD31 (Clone 738)	Bioss USA	Cat#bs-0468R-A488
Alexa 647 Rabbit anti-human FAPA (Clone 760)	Bioss USA	Cat#bs-5758R-A647
Texas Red mouse anti-human CD4 (Clone RFT-4g)	Abcam	Cat#ab51387, RRID AB_868929
FITC Rat anti-human FOXP3 (Clone PCH101)	eBioscience	Cat# 11-4776-42, RRID: AB_1724125
Alexa 647 rat anti-human MAC-2 (Clone M3/38)	BioLegend	Cat#125408, RRID: AB_1186110
Anti-Glucose 6 Phosphate Dehydrogenase antibody	Abcam	Cat#Ab993, RRID: AB_296714
Anti-rabbit IgG, HRP-linked Antibody	Cell Signaling	Cat#7074S, RRID: AB_2099233
Biological Samples		
Mouse liver and muscle tissue from C57BL7 male mice	Medical University of Vienna, Center for Biomedical Research, Division of Laboratory Animal Science and Genetics	N/A
Healthy and cancerous human colon tissue	Medical University of Vienna, Department of Surgery	N/A
Breast Cancer Tissue Array Frozen	BioChain	Cat#T6235086
Chemicals, Peptides, and Recombinant Proteins		
Tissue-Tek O.C.T. Compound	Sakura	Cat#4583
Trizma Maleate	Sigma-Aldrich	Cat#T3128
Poly(vinyl alcohol) Mw 89,000-98,000	Sigma-Aldrich	Cat#341584
1-Methoxy-5-methylphenazinium methyl sulfate	Sigma-Aldrich	Cat#M8640
Sodium Azide	Sigma-Aldrich	Cat#S2002
Nitroblue Tetrazolium chloride	Sigma-Aldrich	Cat#N6876
Phenazine methosulfate	AppliChem	Cat#A2212
D-Glucose 6-phosphate solution	Sigma-Aldrich	Cat#G7772
DL-Glyceraldehyde 3-phosphate diethyl acetal barium salt	Santa Cruz Biotechnology	Cat#sc-214937
β-Nicotinamide adenine dinucleotide hydrate	Sigma-Aldrich	Cat#N1511
Sodium L-Lactate	Sigma-Aldrich	Cat#71718
β-Nicotinamide adenine dinucleotide phosphate hydrate	Sigma-Aldrich	Cat#N5755
Isocitric acid trisodium salt hydrate	Sigma-Aldrich	Cat#I1252
Sodium Succinate dibasic	Sigma-Aldrich	Cat#14160
trans-Dehydroandrosterone	Sigma-Aldrich	Cat#D4000
Sodium Iodoacetate	Sigma-Aldrich	Cat#I2512
Sodium oxamate	Sigma-Aldrich	Cat#O2751

(*Continued on next page*)

Continued

REAGENT or RESOURCE	SOURCE	IDENTIFIER
Malonic acid	Sigma-Aldrich	Cat#M1296
Oxaloacetic acid	Sigma-Aldrich	Cat#O4126
Mowiol 4-88	Sigma-Aldrich	Cat# 81381
4′,6-Diamidino-2-phenylindole dihydrochloride (DAPI)	Sigma-Aldrich	Cat#32670
Complete protease inhibitor cocktail	Roche	Cat#11697498001
PhosStop phosphatase inhibitor cocktail	Roche	Cat#04906845001
D-(+)-Glucose solution	Sigma-Aldrich	Cat#G8769
5-Cyano-2,3-Ditolyl Tetrazolium Chloride	Sigma-Aldrich	Cat#94498
MitoTracker Green FM	Thermo Fisher Scientific	Cat#M7514
Trizol	Ambion	Cat#15596026
Glycogen (RNase free)	Peqlab	Cat#37-1810
Critical Commercial Assays		
2D WB ZOOM IPGRunner Combo Kit & Novex ZOOM gel System	Life Technologies	Cat#ZM0001, ZM0002,EC60261BOX
NativePAGE Novex Bis-Tris Gel System	Life Technologies	Cat#BN2007, BN2008, BN2001, BN2002,NP0336BOX, LC0725
Seahorse XF24 Islet Capture Microplates	Seahorse Bioscience	Cat#101122-100
High Capacity cDNA Reverse Transcription Kit	Applied Biosystems	Cat#4368813
GoTag qPCR Master Mix	Promega	Cat#A6002
Oligonucleotides		
mLdha_1 Forward GAGCTTCCATTTAAGGCCCC; Reverse: TCATCCGCCAAGTCCTTCATT	This paper	N/A
mLdha_2 Forward: GAGCAACTTGGCGCTCTACT; Reverse: CTCATCCGCCAAGTCCTTCAT	This paper	N/A
mLdhb_1 Forward: GTGGTGGACAGTGCCTATGA; Reverse: GTAGACACGGGGTGAATCCG	This paper	N/A
mLdhb_2 Forward: GGTGGACAGGGAATGTACGG; Reverse: GAGCGACCTCATCGTCCTTC	This paper	N/A
mIDH3a Forward: TTGCTGGTGGTGTTCAGACA; Reverse: ATTGCTGTGACATTGCGCTC	This paper	N/A
mIDH3b Forward: CATGCTGCGGCATCTCAATC; Reverse: GTCTCGAGTCCGTACCTTGC	This paper	N/A
mIDH3g Forward: GCTGCAAAGGCAATGCTCAA; Reverse: GGAGGAATTGTTTGTTGTGAGGA	This paper	N/A
mHPRT Forward: CGCAGTCCCAGCGTCGTG; Reverse: CCATCTCCTTCATGACATCTCGAG	This paper	N/A
Software and Algorithms		
Fiji	N/A	https://fiji.sc/
HistoQuest	TissueGnostics Austria	http://www.tissuegnostics.com/en/products/analysing-software/histoquest
TissueQuest	TissueGnostics Austria	http://www.tissuegnostics.com/en/products/analysing-software/tissuequest
Tm4 Multi Experiment Viewer	N/A	http://mev.tm4.org/

(*Continued on next page*)

Continued

REAGENT or RESOURCE	SOURCE	IDENTIFIER
Metlab 8.3	MathWorks	https://www.mathworks.com/products/matlab.html
Primer-BLAST	N/A	https://www.ncbi.nlm.nih.gov/tools/primer-blast/
Primer-3	N/A	http://primer3.ut.ee/
UCSC In-Silico PCR	N/A	http://rohsdb.cmb.usc.edu/GBshape/cgi-bin/hgPcr
GraphPad Prism	GraphPad	https://www.graphpad.com/
Other		
Superfrost Plus Microscope Slides	Thermo Fisher Scientific	Cat#7951PLUS

CONTACT FOR REAGENT AND RESOURCE SHARING

Further information and requests for resources and reagents should be directed and will be fulfilled by the Lead Contact, Arvand Haschemi (arvand.haschemi@meduniwien.ac.at).

EXPERIMENTAL MODEL AND SUBJECT DETAILS

Tissue Samples

Liver and muscle tissue used for basic characterization of the assays were harvested from 12 week old male C57BL/6N mice. Tissue samples of fed (*aa libitum*), fasted (over-night) and after glucose administration by oral gavage (2 g/kg) were obtained from a set of 8 week old male C57BL/6J mice. Mice purchased from Charles River (C57BL/6N) or the Jackson Laboratory (C57BL/6J) were bred in-house and maintained under conventional housing conditions in a temperature- and humidity-controlled mouse facility on a 12-h light-dark cycle at the Center for Biomedical Research, Medical University of Vienna, according to institutional guidelines. Mice were housed with 5 mice per cage and fed *ad libitum* with regular chow diet produced by ssniff Spezialdiäten GmbH.

Human colon test samples were obtained from a 53 year old male patient suffering from a tubular adenocarcinoma located in the caecum. Matched healthy control tissue was removed about 10 cm from the tumor side. The patient did not receive any neoadjuvant treatment prior surgery. Pathologically, the cancer was resected *in toto* (R_0), had grown into the outermost layers of the colon (T_3), showed lymphatic invasion (L_1), had spread to 1 out of 37 examined lymph nodes (N_{1a}) but had not metastasized to a distant organ (M_0) and showed no vascular (V_0) or perineural invasion (P_{n0}). Moreover, the tumor was moderately differentiated (G_2) and classified as stage IIIB according to the Union for International Cancer Control-Tumor Node Metastasis (UICC-TNM) classification. Genetically, the tumor was wild-type for *NRAS* (Neuroblastoma RAS viral oncogene homolog) and *BRAF* (serine/threonine-protein kinase B-Raf), but *KRAS* (V-Ki-ras2 Kirsten rat sarcoma viral oncogene homolog) was mutated on codon 146 and *PIK3CA* (phosphatidylinositol-4,5-bisphosphate 3-kinase) was mutated in the kinase domain on exon 20. This study was conducted according to protocols approved by Austrian government committee on animal experimentation and the Ethical Committee of the Medical University of Vienna.

Breast Cancer Tissue Array

The Breast Tumor Frozen Tissue Array slides contained 3 control tissue-biopsies from healthy individuals and 37 tissues from breast cancer patients, consisting of 2 invasive lobular- and 35 invasive ductal carcinoma specimens with information on their ER, PR and HER2 status. In total, the array comprised of 6 specimens which were ER^+, 3 specimens which were PR^+, 7 specimens which were $HER2^+$, 9 specimens which were ER^+/PR^+, 2 specimens which were $PR^+/HER2^+$ and 10 specimens which were negative for all three markers (triple negative). Two specimens which were invasive lobular carcinomas, the two $PR^+/HER2^+$ specimens, one ER+/PR+ specimen because it was missing on one slide and two triple negative specimens because they did not include any FAP^+ or $ki67^+$ cells were excluded from further analysis.

METHOD DETAILS

Metabolic Imaging

Histochemical Detection of Enzymatic Activities

The enzyme histochemical procedures were based on the protocols of van Noorden and Frederiks (1992). Briefly, tissues were harvested, cut in 100 mm^2 pieces, snap-frozen in O.C.T. Compound and stored at −80°C. After temperature compensation for ten minutes, the tissue blocks were trimmed in a cryostat chamber to the desired level and cut in 6 μm thickness at slow and constant speed and picked up on Superforst microscopy slides. Slides were stored at −80°C for at least 24 hours.

For the enzyme activity assays/stainings, enzyme specific buffers were prepared as follows: For the G6PD, LDH and IDH3 assays the buffer was 0.1 M Tris-Maleate buffer pH 7.5, for the detection of GAPDH activity it was 0.1 M Tris-Maelate buffer pH 8.0 and for the SDH activity assay it was 0.1 M Tris-HCl buffer pH 8.0. In these enzyme specific buffers, ten percent polyvinyl alcohol was dissolved stirring in a water bath at 60°C until the mixture was clear. The solution was stored in air-tight vials at 60°C. For the activity stainings, the assay media were freshly prepared and contained for G6PD, GAPDH and LDH activity assays 0.45 mM methoxyphenanzine methosulfate, 5 mM sodium azide and 5 mM nitroblue tetrazolium chloride (pre-dissolved in 50% ethanol and 50% dimethylformamide and heated to 60°C). The assay media for mitochondrial IDH3 and SDH activities contained 0.2 mM phenanzine methosulfate instead of methoxyphenanzine methosulfate. The assay media also contained 15 mM G6P, 0.8 mM NADP+ and 4 mM MgCl for the analysis of G6PD activity; 2.5 mM glyceraldehyde-3-phosphate (pre-dissolved in 0.01M HCl) and 3 mM NAD+ for the analysis of GAPDH activity; 150 mM sodium lactate and 3 mM NAD+ for the analysis of LDH activity; 100 mM isocitric acid, 7 mM NAD+ and 10 mM MgCl for the analysis of IDH3 activity; 60 mM sodium succinate for the analysis of SDH activity. Negative control reactions were performed in absence of substrate or presence of 80 mM DHEA (for G6PD inhibition), 40 mM sodium iodoacetate (for GAPDH inhibition), 200 mM sodium oxamate (for LDH inhibition), 100 mM oxaloacetic acid (for IDH3 inhibition) or 250 mM malonic acid (for SDH inhibition). Enzyme inhibitors were applied at very high concentrations for maximum inhibition, irrespective of enzyme selectivity concerns as the reaction specificity of the activity assays are defined by the provided substrates.

Immediately before performing the experiment, tissue sections were defrosted for two minutes at room temperature. Assay medium containing the enzyme-specific substrate and coenzymes was applied to cover the whole tissue section. Enzyme reactions were carried out protected from light at room temperature under gentle shaking for 15 min. For enzyme kinetics in Figures 1B–1D substrate concentrations and incubation times were as indicated in the figure legend. Slides were washed twice in 60°C PBS for one minute and once in 4°C PBS for three minutes to remove the incubation media and stop the reaction. Tissue sections were either directly dried and mounted in Mowiol 4-88 or further used for antibody stainings.

For analysis of the breast cancer tissue array, four consecutive slides were stained for LDH, GAPDH, SDH and G6PD activities in combination with antibody stainings and DAPI. One slide of the array was stained with hematoxylin and eosin (H&E) and mounted in Entellan according to established protocols.

Immunofluorescence

Immediately after the enzyme activity stainings, tissue sections were blocked for 30 min with a 3% bovine serum albumin blocking solution containing 0.01% Triton X-100. Sections were then either stained for one hour at room temperature with directly labeled antibodies or no antibodies to control for background staining with gentle shaking. Next, slides were washed two times for three minutes in PBS and stained 5 min with DAPI. After washing again three times with PBS containing 0.01% Tween 20, tissue sections were dried and mounted in Mowiol 4-88.

Image Acquisition and Analysis

TissueFAXS acquisition was performed using a Zeiss Observer Z1 microscope equipped with a stage for 12-slides, a Hamamatsu Photonics Orca flash 4.0 Camera and a X-Cite Series 120PCQ Laser assembled by TissueGnostics, Austria. All images were acquired using the TissueFAXS 4.0 Slides software by TissueGnostics. Preview settings were adjusted according to the manufacturer's recommendation with a 2.5x objective. Acquisition was performed using a 20x objective. Filters for DAPI, FITC, Cy5, Texas Red, Cy7 and TL were used to detect respective fluorescent signals. Exposure times were adjusted individually for each filter, but once adjusted kept constant for the entire experiment. In the software, the autofocus used a manual focus search algorithm with variance rough focus measurements. Fine focus was set at High Performance with x and y at 50%. The utilized focus strategy scanned three pictures in height and three pictures in width and used a floating focus point. The focus interval was set after manual focusing around the current z position.

For the analysis of brightfield images, the formazan formation was analyzed using the HistoQuest 4.0.4.0150 software. Formazan intensities were analyzed in the various shapes 2.0 modes detecting area (μm^2), mean intensity and sum intensity. The color picker tool was used to individually define monoformazan (pink shades) and diformazan (purple shades) formation. The reaction velocity V for each enzyme (Figure 1F; Figure S1C) was calculated by GraphPad Prism 5.0 based on the slopes of formazan formation, measured in relative intensities, after 5, 10, 15 and 20 min of incubation for indicated substrate concentrations.

For the analysis of fluorescent images, the brightfield pictures of the formazan formation were first inverted with Fiji and then analyzed by TissueQuest 4.0.1.0128 software. DAPI was set as the master marker in the various shape mode 2.0. Contaminations of the specimen as well as turned down tissue were excluded manually from analysis. The analysis of DAPI was set to the default settings, with an automated background threshold. The cell detection parameters were set to a maximum exterior radius of 7μm. The raw data, containing all relative intensities for each event (cell), was exported to Excel to calculate the frequency-distributions and the respective *mean enzyme activities* as relative formazan intensities formed per 15 min per cell. The exported data was also used in GraphPad Prism to create histograms and scatter-blots.

For analysis of the breast cancer tissue array, the tumor bulk was identified via an H&E staining on a separate slide and in the HistoQuest software the selected regions were transferred to the corresponding fluorescence images in the TissueQuest software and corrected manually.

Confocal Laser Scanning Microscopy

For confocal co-localization of enzymatic activity with MitoTracker we used 5-Cyano-2,3-di-(p-tolyl)tetrazolium chloride (CTC) as previously reported instead of NBT (Frederiks et al., 2006). Briefly, the tissue sections were incubated for 15 min in the dark in

IDH3 assay buffer containing 100 mM isocitric acid, 7 mM NAD+ and 10 mM MgCl, 0.2 mM phenanzine methosulfate, 5 mM sodium azide and 5 mM CTC (pre-dissolved in 50% ethanol and 50% dimethylformamide and heated to 60°C). The negative control reactions were performed in presence of 100 mM oxaloacetic acid. After washing in PBS, MitoTracker was added for 10 min at room temperature in the dark according to the manufacturer's recommendations. Nuclei were stained 5 min with DAPI. Slides were mounted with mowiol and the specimens were immediately examined using a Zeiss LSM780 laser scanning Microscope (Carl Zeiss Optics). The setting of the pinhole was corresponding with 1 Airy disc. DAPI was imaged with 405nm excitation and detection at a bandwidth of 410-488nm, CTC was imaged with excitation at a wavelength of 488nm and the fluorescence was measured at an emission bandwidth of 620-758nm, MitoTracker was imaged with 488nm excitation and detection at a bandwidth of 489-551nm.

Western Blots

Western blots were performed according to standard protocols. Briefly, mouse liver and muscle tissue was harvested, snap frozen and kept at −80°C. Tissues were homogenized in RIPA buffer (50 mM Tris-HCl pH 7.6, 150 mM NaCl, 1 mM EDTA, 1% Triton X-100, 1% Na-deoxycholate, 0.1% SDS) supplemented with Complete protease inhibitor cocktail and PhosStop phosphatase inhibitor cocktail. Tissue debris were removed by centrifugation (16000 g, 10 min, 4°C) and the protein concentration in the supernatant determined using a BCA protein assay kit.

After adjustment of the total protein concentration in the samples, discontinuous Tris-glycine SDS-PAGE page was performed using 12% separating gels and 6% stacking gels. The samples were loaded in Laemmli-buffer (2% SDS, 5% 2-mercaptoethanol, 10% glycerol, 0.002% bromphenol blue, 0.0625 M Tris-HCl, pH 6.8) and heated to 95°C for 10 min. The gels were run at constant voltage (stacking gel 60 V, separating gel 100 V), using a pre-stained Page Ruler Plus ladder for size estimation. The proteins were transferred to PVDF membranes at a constant voltage of 12 V overnight. After blocking, the membranes were incubated with a primary rabbit anti-G6PD-antibody, washed with TBS-T and incubated with a secondary HRP-coupled antibody. Development of the blots was carried out using Super Signal West Pico chemiluminescent substrate according to the manufacturer's protocol. Signal detection was performed using a high performance chemiluminescence film upon exposure of 3 min and development in an AGFA developing and fixation chamber (AGFA Healthcare). To indicate equal loading (25μg/lane), Coomassie staining was performed to detect total protein levels according to the standard protocols using a Coomassie staining solution (0.1% Coomassie G-250, 20% Methanol, 10% acid).

For the 2D Western Blots, isoelectric focusing was conducted with 150 μg of precipitated proteins resolved in a urea buffer to rehydrate gel-strips with a pH range of 4-7 according to the manufacturers manual. After equilibration of the strips with 100 mM DTT for 10 min and 2% iodoacetamide, proteins were resolved on a 12% polyacrylamide gel and transferred to PVDF membranes. G6PD was detected as described above.

G6PD In-Gel Activity Assay

The G6PD in-gel activity assays were performed according to standard protocols (Ninfali et al., 1997). Briefly, tissues were harvested as described for western blots and homogenized using the Native PAGE-sample preparation kit according to the manufacturer's instructions. Briefly, the samples were homogenized in the Native PAGE sample buffer supplemented with 1% Digitonin, Complete protease inhibitor cocktail and PhosStop phosphatase inhibitor cocktail. The supernatant was cleared by centrifugation and sonicated (3x 15 s) on ice. The protein concentration in the supernatant was detected using the BCA protein assay kit. Native PAGE was performed using the Native Page system with Novex Nu-Page 4%–12% Zoom gels according to the manufacturer's instructions.

All steps for the in-gel enzyme activity assay were conducted at room temperature. For the G6PD activity staining, the gel was incubated in 50 mL of 50 mM potassium phosphate buffer (pH 7.5) containing 15 mM G6P, 0.8 mM NADP+, 4 mM MgCl, methoxyphenanzine methosulfate, 5 mM sodium azide and 5 mM nitroblue tetrazolium chloride. Control reactions were carried out in absence of substrate. The reactions were performed overnight and were stopped by fixing the gel for 30 min in a solution containing 50% methanol and 10% acetic acid. This was followed by a long-term preservation of the gel in 10% methanol and 8% acetic acid at 4°C.

G6PD Activity Assay in Tissue Homogenates

Spectrophotometric detection of G6PD activity was conducted according to standard protocols (Glock and McLean, 1953). Briefly, mouse liver and muscle tissue was harvested, snap frozen and kept at −80°C. Tissues were homogenized in a G6PD stabilizing buffer (50 mM Tris pH 7.5; 1 mM EDTA and 0.002% Triton X-100) as indicated above. Tissue debris was removed by centrifugation (16000 g, 10 min, 4°C) and the protein concentration in the supernatant was determined by using the BCA protein assay kit. The G6PD activity of 100 μg crude protein was assessed in a buffer consisting of 50 mM Tris pH 7.8, 65 mM MgCl, 0.38 mM NADP+ and varying concentrations of G6P by the power of 10 from 0,15 mM to 150 mM. All components were added into a 1 mL quartz cuvette, mixed for 15 s and formation of NADPH measured at 340 nm for 20 min at room temperature using a Hitachi U-2900 spectrophotometer. Enzymatic activities were measured by monitoring the accumulation of NAPDH over time (1 Unit = 1 μmol NADPH min^{-1}).

RNA Isolation, cDNA Synthesis, and Real-Time Quantitative PCR

Muscle tissue RNA was isolated using TRIzol according to the standard protocol and glycogen was added as a carrier to increase RNA yields. Briefly, the tissue was homogenized in TRIzol reagent on ice and the RNA-containing supernatant was cleared from tissue debris. After adding chloroform, the lysates were mixed by inverting and the RNA-containing aqueous phase was transferred

into a fresh tube and glycogen was added. RNA was precipitated by isopropanol and the RNA-pellet was washed and air-dried. The RNA was resuspended in RNase-free water and solubilized at 55°C for 15 min. RNA concentration was determined and 500μg of total RNA was subjected to reverse transcription using the High Capacity cDNA Reverse Transcription kit according to the manufacturer's instructions. The resulting cDNA-solution was diluted and quantitative real time PCR was performed using the GoTaq-qPCR master mix according to the standard protocol with a BioRad CFX96/C1000-Real time thermal cycler system. Cycling conditions were the following: initial denaturation (95°C, 2min.), followed by 45 cycles of denaturation (95°C, 15 s) and annealing/elongation (60°C 60 s). For normalization, threshold cycles (Ct-values) of all replicate analyses were normalized to Hypoxanthine-guanine phosphoribosyltransferase (HPRT) within each sample to obtain sample-specific ΔCt values. To compare the effects of treatments with controls, 2-ΔΔCt values were calculated to obtain fold expression levels.

Cellular Respiration and Extracellular Acidification

The Seahorse XF24 Extracellular Flux Analyzer was used to determine the bio-energetic profile of intact tissue samples. Immediately after surgical removal of the tissue, healthy and cancerous colon tissue was punched out with a disposable 3 mm biopsy needle (Kai medical), tissue pieces were weighted, placed into XF24 Islet Capture Microplates and covered with the XF Islet Capture Screen Insert and coated with glucose-containing media. Oxygen consumption rate (OCR) and extracellular acidification rate (ECAR) were assessed immediately and normalized per mg tissue.

QUANTIFICATION AND STATISTICAL ANALYSIS

Heatmaps and Correlation Analysis

Heatmaps were created using the Tm4 Multi Experiment Viewer. For correlation analysis the data was imported into MATLAB 8.3. Five missing values (1.39% of the overall data) were replaced by the mean value of the same property over the other patients. The pairwise Pearson correlation coefficients between all patients were calculated for LDH activity, resulting in a 30x30 correlation matrices. A hierarchical cluster tree based on the highest correlations within the matrix was built.

Statistical Analysis

Respective statistical analyses are indicated in the figure legends. Unless otherwise stated, statistical comparisons were performed using unpaired two-tailed Student's t tests and results are indicated in the individual figures (* = $p < 0.05$, ** = $p < 0.01$, *** = $p < 0.001$). Statistical analyses were generated in GraphPad Prism 5 Software.